J. Fluid Mech. (2025), *vol.* 1011, A48, doi:10.1017/jfm.2025.402

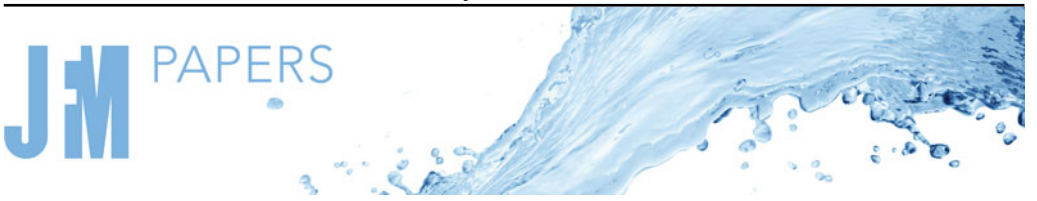

Confinement-induced spreading and fingering of suspensions

Rui Luo[1], **Maxwell Marshall**[2], **Zilong He**[3], **Li Wang**[4] **and Sungyon Lee**[3]

[1]Engineering Science and Applied Mathematics, Northwestern University, Evanston, IL, USA

[2]SICK Sensor Intelligence, Minneapolis, MN, USA

[3]Department of Mechanical Engineering, University of Minnesota, Minneapolis, MN, USA

[4]School of Mathematics, University of Minnesota, Minneapolis, MN, USA

Corresponding author: Sungyon Lee, sungyon@umn.edu

(Received 24 October 2024; revised 11 April 2025; accepted 12 April 2025)

Viscous fingering, a classic hydrodynamic instability, is governed by the the competition between destabilising viscosity ratios and stabilising surface tension or thermal diffusion. We show that the channel confinement can induce 'diffusion'-like stabilising effects on viscous fingering even in the absence of interfacial tension and thermal diffusion, when a clear oil invades the mixture of the same oil and non-colloidal particles. The key lies in the generation of long-range dipolar disturbance flows by highly confined particles that form a monolayer inside a Hele-Shaw cell. We develop a coarse-grained model whose results correctly predict universal fingering dynamics that is independent of particle concentrations. This new mechanism offers insights into manipulating and harnessing collective motion in non-equilibrium systems.

Key words: Hele-Shaw flows, particle/fluid flows

1. Introduction

Viscous fingering (Saffman & Taylor 1958; Homsy 1987) occurs when a less viscous fluid displaces a more viscous fluid inside porous media. First discovered in oil recovery processes, viscous fingering has been studied extensively as a premier example of a pattern-forming system whose fundamental physics has aided our understanding of solidification and other growth phenomena (Couder 2000). Viscous fingering is driven by the viscosity difference between the two fluids, while the interfacial tension γ stabilises the system, setting the critical wavelength that scales as $\gamma^{1/2}$ (Chuoke, Van Meurs &

Van Der Poel 1959; Park, Gorell & Homsy 1984; Park & Homsy 1984). In the limit of zero interfacial tension, the instability between the two fluids is mediated by thermal diffusion characterised by the Péclet number *Pe*, the ratio of flow advection to diffusion. For relatively small pore-scale *Pe* where diffusion homogenises the flow within the pore, viscous fingering can be described by a depth-averaged two-dimensional (2-D) model (Tan & Homsy 1986; Booth 2010; Nijjer, Hewitt & Neufeld 2018). In such systems, thermal diffusion determines the mixing region width and sets the wavelength of instability (Wooding 1962; Hickernell & Yortsos 1986; Yortsos & Salin 2006; Booth 2010; Nijjer *et al.* 2018).

In this paper, we uncover a new mechanism of wavelength selection of viscous fingering in the limit of zero interfacial tension and $Pe \to \infty$, with the use of a 2-D suspension. We experimentally inject clear oil into the mixture of the same oil and non-colloidal particles inside a rectangular Hele-Shaw cell, whose gap thickness is comparable to the particle diameter. The inclusion of the particles in the oil increases the effective viscosity of the mixture (Einstein 1906; Brady 1983) and generates the necessary condition for viscous fingering. Despite the absence of thermal diffusion, our experiments reveal a striking similarity to 2-D viscous fingering with miscible liquids at low *Pe* (Tan & Homsy 1986). The invading oil is shown to finger into the suspension, and the characteristic finger width gradually widens over time. This behaviour is a complete departure from the suppression of fingering that is observed when a clear oil invades the suspension inside the channel with a large gap (Luo, Chen & Lee 2020).

The key feature responsible for this surprising phenomenon is the channel confinement that causes the flow disturbance by each particle to behave as a long-range dipole. Such non-equilibrium many-body systems with slowly decaying disturbances have been shown to exhibit complex collective dynamics, including hydrodynamic fluctuations of 2-D uniform suspension flows (Desreumaux *et al.* 2013), and clustering of magnetically driven micro-rollers (Driscoll *et al.* 2017). To demonstrate this, we derive a coarse-grained model accounting for the dipolar interactions between particles, whose results correctly predict the development of gradually widening fingers even at $Pe \to \infty$. Our model further reveals universal fingering dynamics that is independent of the initial particle concentration, which only sets the time-scale of the instability.

The paper is organised as follows. We introduce the experimental set-up and observations in § 2, while the formulation of the mathematical model is included in § 3. We discuss the model results and make the quantitative comparison with the experiments in § 4. In § 4.3, we uncover the physical origin of wavelength selection. Finally, we conclude the paper with the summary and discussion in § 5.

2. Experiments

To induce viscous fingering with zero interfacial tension, we inject silicone oil (density $0.96\,\mathrm{kg\,m^{-3}}$, dynamic viscosity $\mu = 0.096\,\mathrm{Pa\,s}$) into the mixture of the same oil and polyethylene particles with diameter $d = 0.625 \pm 0.4\,\mathrm{mm}$ and density $\rho_p = 0.98\,\mathrm{g\ cm^{-3}}$ inside a rectangular Hele-Shaw cell. Since $Pe \sim O(10^{10})$, the thermal diffusion of the non-colloidal particles is negligible. As illustrated in figure 1(*a*), the Hele-Shaw cell comprises two glass plates with width $W = 60\,\mathrm{mm}$ separated by gap thickness $b = 0.76 \pm 0.03\,\mathrm{mm}$, such that $b/d \approx 1$ ensures the formation of a monolayer.

In our experiments, we fix the oil flow rate to $Q = 3.62\,\mathrm{ml\ min^{-1}}$, and systematically vary the particle volume fractions ϕ_i or the corresponding average number densities ρ_i. Note that the average number density ρ_i is defined as the total number of particles over the area of the domain. Varying ϕ_i or ρ_i is equivalent to varying the viscosity ratio between

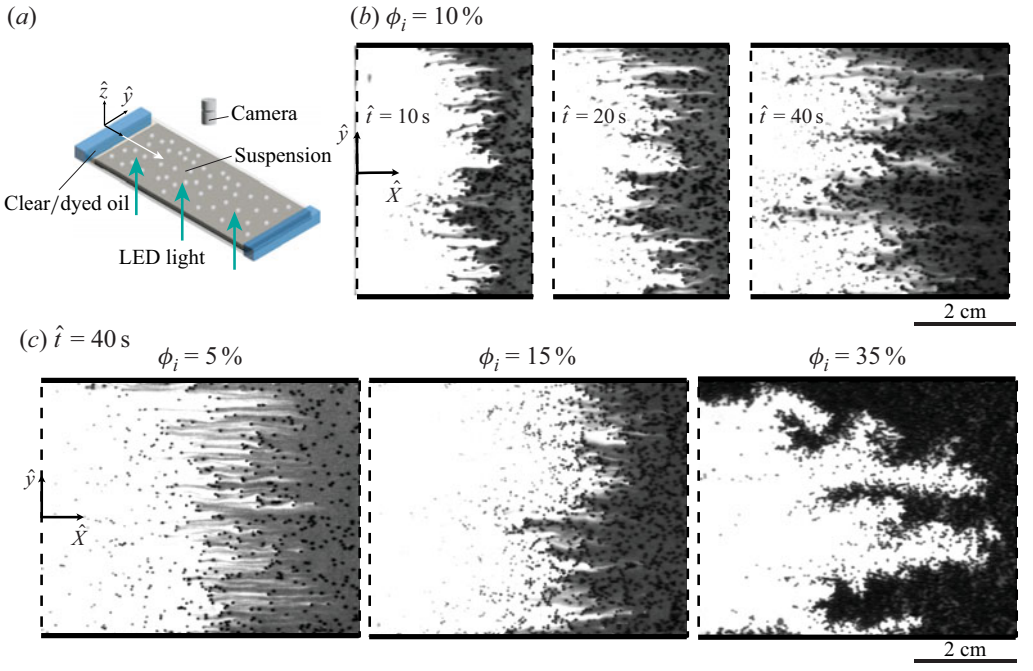

Figure 1. (*a*) Schematic of the experimental set-up: a 2-D Hele-Shaw cell consisting of two rectangular glass plates that are separated by a thin gap. The images of flow patterns are captured from above using a CMOS camera, as the clear oil invades the particle–oil mixture. (*b*) The time-sequential experimental images at $\phi_i = 10\,\%$ show the gradual widening of fingers over time in a single experiment. (*c*) The experimental images at $\hat{t} = 40$ s show the increase in the critical wavelength λ_c as the initial concentration ϕ_i is increased: $\phi_i = 5\,\%$, $15\,\%$, $35\,\%$. The solid line represents the location of the side wall.

the suspension (defending fluid) and the clear oil (invading fluid); viscosity ratios greater than 1 are conducive to viscous fingering. We estimate the viscosity ratio of the current system based on the following empirical expression of the effective viscosity (Brady 1983): $\mu_{eff} \approx \mu[1 + \rho_i(\pi d^2/2)]$, which is valid for a 2-D suspension in a dilute regime. The resultant viscosity ratios in the current experiments range from 1.2 to 1.8.

Successful experiments require generating a uniform suspension of ϕ_i and a relatively uniform front of invading oil. We include the detailed description of our experimental procedure in Appendix A. We conduct two complementary sets of experiments with and without dyeing the invading oil for the purposes of visualisation. The experiments in which we dye the invading oil allow us to directly visualise the miscible displacement pattern of the invading oil (see figure 1*b*,*c*), while we track the motion of individual particle with corresponding high-resolution experiments with no dyed oil.

The experimental images in figure 1 demonstrate two major observations from the experiments. First, the invading oil is observed to form fingers into the suspension for all ϕ_i or ρ_i tested. Second, the characteristic finger width λ_c (as quantified in Appendix B) increases with both time and ρ_i. The experimental images in figure 1(*b*) demonstrate coarsening of the finger width over time at $\phi_i = 10\,\%$ ($\rho_i = 0.48\ \mathrm{mm}^{-2}$), while at fixed time, fingers of the invading oil appear wider as ρ_i is systematically increased from $5\,\%$ ($\rho_i = 0.17\ \mathrm{mm}^{-2}$) to $35\,\%$ ($\rho_i = 1.84\ \mathrm{mm}^{-2}$) in figure 1(*c*).

The appearance of miscible fingering at all ϕ_i is a clear deviation from the recent series of studies on the displacement of miscible fluids at $Pe \to \infty$ (Goyal & Meiburg 2006; Bischofberger, Ramachandran & Nagel 2014; Nijjer *et al.* 2018; Videbæk & Nagel 2019;

Videbæk 2020). These studies show that the displacement of miscible fluids is stable at low viscosity ratios, including in the case of clear oil invading a suspension (Luo *et al.* 2020). The cause of stable displacements is understood to be the development of a three-dimensional (3-D) structure inside the thin gap at $Pe \to \infty$. Hence by working with highly confined particles whose dynamics can be modelled as quasi-2-D, the onset of fingering is no longer delayed even at low viscosity ratios. Here, we refer to the particles in a monolayer as being 'highly confined' by the channel walls. Yet the emergence of a finite wavelength that evolves with time and ϕ_i speaks to the existence of an alternate wavelength selection mechanism, which we will rationalise with a minimal model.

3. Theoretical model

Given the simplicity of our experimental system with no interfacial tension and thermal diffusion, we hypothesise that the hydrodynamic interactions between the highly confined particles comprise both stabilising and destabilising effects, and thereby can describe the observed fingering phenomena. To demonstrate this, we develop a coarse-grained continuum model that takes into account pairwise interactions between particles immersed in the Stokes flow and the initial jump in particle concentrations.

We model our system comprising N particles denoted with the index i $(i = 1, \ldots, N)$. Due to the friction of the bounding walls, a highly confined particle i moves slower than the local oil flow, such that $\hat{\boldsymbol{v}}_{p,i} = \kappa \hat{\boldsymbol{v}}$, where $\hat{\boldsymbol{v}}_{p,i}$ and $\hat{\boldsymbol{v}}$ are the in-plane velocities of the particle and suspending oil in the absence of the particle i, respectively. Here, $\kappa < 1$ is an empirical constant whose value we determine by measuring the velocity of individual particles in dilute suspension experiments. The velocity difference between the particle and the fluid causes a dipolar disturbance to the suspending oil, $\hat{\boldsymbol{v}}^{dip}$. The dipolar disturbance introduced at position $\hat{\boldsymbol{r}}$ by a particle at $\hat{\boldsymbol{r}}'$ can be modelled as $\hat{\boldsymbol{v}}^{dip}(\hat{\boldsymbol{r}}, \hat{\boldsymbol{r}}') = S\,\hat{\boldsymbol{\nabla}}((\hat{\boldsymbol{r}} - \hat{\boldsymbol{r}}') \cdot \boldsymbol{e}_{\hat{X}} / \left|\hat{\boldsymbol{r}} - \hat{\boldsymbol{r}}'\right|^2)$, where S represents the dipolar strength accounting for channel confinement and particle surface properties (Beatus *et al.* 2006, 2012), and $\boldsymbol{e}_{\hat{X}}$ is the unit vector in the axial coordinate $\hat{X}$. The resultant streamlines of $\hat{\boldsymbol{v}}^{dip}$ are symmetric in the transverse direction and asymmetric in the flow direction. We assume that the dipolar disturbances between particles are pairwise additive, such that $\hat{\boldsymbol{v}} = \hat{\boldsymbol{v}}^{\infty} + \sum_{j \neq i} \hat{\boldsymbol{v}}^{dip}(\hat{\boldsymbol{r}}_i, \hat{\boldsymbol{r}}_j)$, where $\hat{\boldsymbol{v}}^{\infty} = \hat{v}^{\infty} \boldsymbol{e}_{\hat{X}}$ is the uniform background flow.

Moving from the individual particle dynamics to a continuum description, we now derive an equation for the local number density $\rho(\hat{\boldsymbol{r}}, \hat{t})$ based on mass conservation:

$$\partial_{\hat{t}} \rho(\hat{\boldsymbol{r}}, \hat{t}) + \hat{\boldsymbol{\nabla}} \cdot \hat{\boldsymbol{j}}(\hat{\boldsymbol{r}}, \hat{t}) = 0, \tag{3.1}$$

where the local particle flux $\hat{\boldsymbol{j}}(\hat{\boldsymbol{r}}, \hat{t})$ is derived using a conventional kinetic theory (Menzel 2012; Desreumaux *et al.* 2013)

$$\hat{\boldsymbol{j}}(\hat{\boldsymbol{r}}, \hat{t}) = \kappa\, \rho(\hat{\boldsymbol{r}}, \hat{t}) \left[\hat{\boldsymbol{v}}^{\infty} + \iint_{|\hat{\boldsymbol{r}} - \hat{\boldsymbol{r}}'| \geq d} \hat{\boldsymbol{v}}^{dip}(\hat{\boldsymbol{r}}, \hat{\boldsymbol{r}}')\, \rho(\hat{\boldsymbol{r}}', \hat{t})\, \mathrm{d}\hat{\boldsymbol{r}}' \right]. \tag{3.2}$$

The quadratic nonlinearity in (3.2) accounts for the pairwise interaction, and introducing the cut-off length in the integration ensures that the number density remains bounded. A similar continuum framework has been used previously to model the collective dynamics in systems comprising multiple bodies, such as magnetic rotors, sedimenting particles and droplet emulsions (Desreumaux *et al.* 2013; Delmotte *et al.* 2017; Sprinkle *et al.* 2021).

We move to a moving reference frame based on $\hat{x} = \hat{X} - \kappa(\hat{v}^{\infty} + \pi S \rho_i)\hat{t}$, where $\hat{x}$ is the moving coordinate in the flow direction, while $\hat{y}$ corresponds to the coordinate in

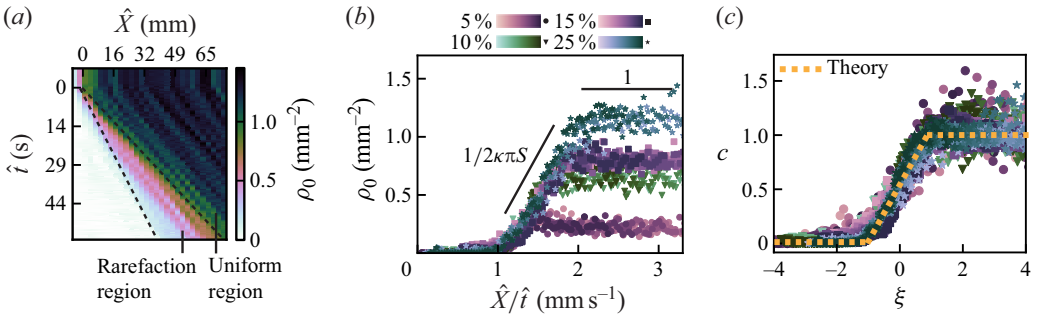

Figure 2. (*a*) Space–time diagram illustrating the number density ρ_0 measured and averaged over the channel width from an experiment at $\phi_i = 25\,\%$ or $\rho_i = 1.13\ \mathrm{mm}^{-2}$. The colour scale indicates the local number density. The rarefaction region (bounded by dashed lines) is characterised by a gradual increase in ρ_0. (*b*) We plot ρ_0 measured from the experiments at $\phi_i = 5\,\%, 10\,\%, 15\,\%, 25\,\%$ as a function of $\hat{X}/\hat{t}$, which reveals the self-similarity of our data and two distinct regions. The rarefaction region, exhibiting a positive slope, is influenced by the system's confinement parameters (κ and S), while the uniform region is set by ϕ_i. The colour of each symbol corresponds to different values of ϕ_i, with the darker shade indicating later dimensional times (see the colourmaps in (*b*)). (*c*) The dimensionless number density profiles c from all experiments collapse onto a single rarefaction solution curve, consistent with the predictions of the leading-order equation (dashed line).

the transverse direction. We define $c \equiv \rho/\rho_i$, and non-dimensionalise (3.1) based on the scales: length d, velocity $\kappa\pi S\rho_i$, and time $d/(\kappa\pi S\rho_i)$. The dimensionless variables will be denoted without hats to clearly distinguish them from the dimensional variables. Notably, the average number density ρ_i sets the intrinsic speed of the system, and thereby the characteristic timescale.

The resultant dimensionless equation for c is

$$\frac{\partial c}{\partial t} + \left(\frac{1}{\pi}u_d - 1\right)\frac{\partial c}{\partial x} + \frac{1}{\pi}v_d\frac{\partial c}{\partial y} - \frac{1}{\pi}c\int_0^{2\pi} c(\boldsymbol{r}-\boldsymbol{n},\,t)\cos\theta\,\mathrm{d}\theta = 0, \tag{3.3}$$

where $\boldsymbol{n} = (\cos\theta, \sin\theta)$, and u_d and v_d are the summed dimensionless disturbance velocities in x and y, respectively:

$$\begin{aligned} u_d(x,\,y) &= \iint_{\tilde{x}^2+\tilde{y}^2\geq 1} \frac{\tilde{y}^2-\tilde{x}^2}{(\tilde{x}^2+\tilde{y}^2)^2} c(x+\tilde{x},\,y+\tilde{y},\,t)\,\mathrm{d}\tilde{x}\mathrm{d}\tilde{y}, \\ v_d(x,\,y) &= \iint_{\tilde{x}^2+\tilde{y}^2\geq 1} \frac{2\tilde{x}\tilde{y}}{(\tilde{x}^2+\tilde{y}^2)^2} c(x+\tilde{x},\,y+\tilde{y},\,t)\,\mathrm{d}\tilde{x}\mathrm{d}\tilde{y}. \end{aligned} \tag{3.4}$$

We include the detailed derivation of (3.3) and (3.4) in Appendix C.

Finally, to simulate the invasion of the clear oil into the uniform suspension, we subject (3.3) to the initial condition $c(x,\,y,\,t=0) = (1)_{x>0}$. The dimensionless governing equation and initial condition for c are completely independent of the initial particle number density ρ_i, which suggests the universal nature of the 2-D suspension in the current configuration. In other words, instead of solving the governing equation for varying parameters, such as ρ_i and channel confinement, one only needs to obtain the solution to the dimensionless equation once and re-normalise the result to describe the invasion of clear oil into the 2-D suspension for different physical parameters.

4. Results

4.1. *Rarefaction wave*

To examine the stability of the system, we decompose c into $c{=}c_0(x,t)+\delta\, c(x,y,t)$, where $|c_0|{\gg}|\delta c|$. Here, c_0 is the normalised particle number density at leading order that is uniform in y. Based on this decomposition and the further assumption that $c_0(x+\tilde{x},t)\approx c_0(x,t)+\partial_x c_0(x,t)\,\tilde{x}$ for $\tilde{x}\in[-1,1]$ (see Appendix D for details), we obtain the following equation for c_0 from (3.3):

$$\frac{\partial c_0(x,t)}{\partial t}+[2c_0(x,t)-1]\,\frac{\partial c_0(x,t)}{\partial x}=0. \tag{4.1}$$

Equation (4.1) can be solved analytically via the method of characteristics, with the similarity variable $\xi\equiv x/t$:

$$c_0(\xi)=\begin{cases}0, & \xi<-1,\\ \dfrac{\xi}{2}+\dfrac{1}{2}, & -1<\xi<1,\\ 1, & \xi>1.\end{cases} \tag{4.2}$$

This solution demonstrates the existence of an expanding rarefaction region that linearly connects the regions of clear oil (i.e. $c_0=0$) and uniform suspension (i.e. $c_0=1$).

To validate (4.2) experimentally, we quantify the particle number density averaged in the transverse direction, $\rho_0(\hat{X},\hat{t})$, from our systematic experiments with clear oil. The high-resolution experiments allow us to track the positions of the individual particles inside the cell over the duration of the experiment. We convert the particle positions into $\rho_0(\hat{X},\hat{t})$ by averaging the number of particles inside a rectangular domain that is a few particle diameters wide. For $\phi_i=25\,\%$ or $\rho_i=1.13\,\mathrm{mm}^{-2}$, the plot of $\rho_0(\hat{X},\hat{t})$ in figure 2(*a*) clearly shows the emergence and expansion of the rarefaction region over which $\rho_0(\hat{X},\hat{t})$ gradually increases from 0 to ρ_i (bounded by dashed lines). We acknowledge that ρ_0 shows some non-uniformities even in the uniform region, while its mean value matches ρ_i. Such non-uniformities are caused by the fluctuations that occur in the flow of a 2-D uniform suspension (Desreumaux *et al.* 2013).

We plot ρ_0 as a function of $\hat{X}/\hat{t}$ for different values of ρ_i in figure 2(*b*). Note that $\hat{X}/\hat{t}=\kappa\pi S\rho_i(\xi+1)+\kappa\hat{v}^{\infty}$ based on our non-dimensionalisation. As predicted by our solution in (4.2), $\rho_0(\hat{X},\hat{t})$ for given ρ_i is shown to collapse across all time, experimentally validating the self-similar nature of the rarefaction region. Furthermore, the slope of the linear part of $\rho_0(\hat{X}/\hat{t})$ corresponds to $1/(2\kappa\pi S)$, independent of ρ_i. Once the dipolar strength S is determined experimentally (i.e. $S\approx 0.178\,\mathrm{mm}^3\,\mathrm{s}^{-1}$) from this slope, we set the dimensionless moving coordinate x for each ρ_i. The resultant plot of ρ_0/ρ_i as a function of $\xi=x/t$ shows a reasonable collapse for all experimental parameters in figure 2(*c*).

4.2. *Universal fingering growth*

To probe the stability of the model system, we set $\delta\, c(x,y,t)\equiv 2\sum_{k=0}^{\infty}\tilde{c}_k(x,t)\cos(ky)$ with wavenumber k, and combine it with (3.3). Then with the subscript k omitted for brevity, we arrive at the following governing equation for $\tilde{c}$:

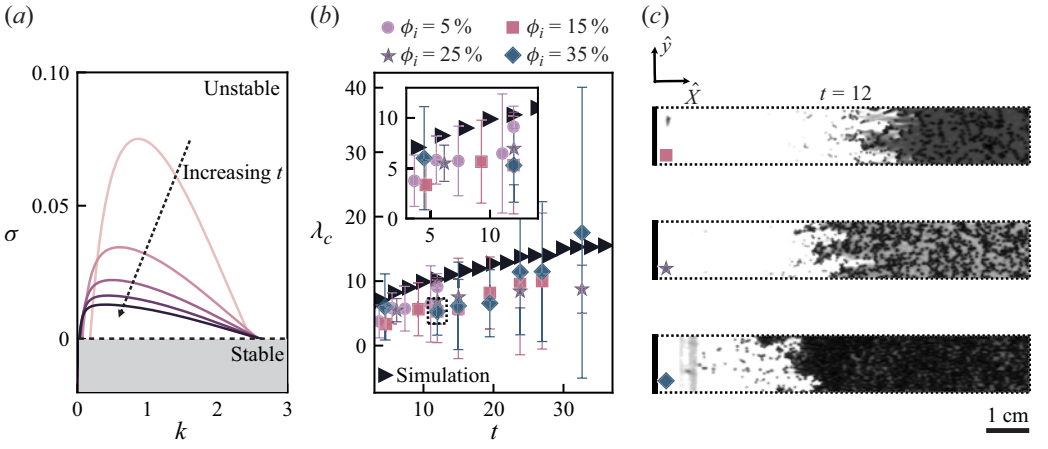

Figure 3. (*a*) The plot of the growth rate σ versus the wavenumber k. The growth rate varies non-monotonically with k, and is positive across a range of wavenumbers. Over time, the critical wavenumber associated with the peak growth rate exhibits a decay. (*b*) The plot of the critical wavelength λ_c over dimensionless time t from the simulations and the experiments; λ_c from the simulations increases over t. Given the universality of the derived equation, the critical wavelengths from different experiments are expected to converge into a single curve upon non-dimensionalisation. The error bars associated with the experimental data reflect the spatial variability of finger widths in the rarefaction region for each experiment. (*c*) We include the experimental images from three experiments ($\phi_i = 5\,\%, 15\,\%, 25\,\%$) at $t = 12$ (or three separate dimensional times). The three images exhibit similar fingering patterns.

$$
\begin{aligned}
0 = {} & \frac{\partial \tilde{c}}{\partial t} - \frac{1}{\pi} c_0 \int_0^{2\pi} \tilde{c}(x - \cos\theta) \cos(-k \sin\theta) \cos\theta \, \mathrm{d}\theta \\
& + \frac{\partial \tilde{c}}{\partial x} \left[\frac{2}{\pi} \int_{-1}^{+1} c_0(x + \tilde{x}) \sqrt{1 - \tilde{x}^2} \, \mathrm{d}\tilde{x} - 1 \right] - \frac{1}{\pi} \tilde{c} \int_0^{2\pi} c_0(x - \cos\theta) \cos\theta \, \mathrm{d}\theta \\
& + \frac{1}{\pi} \frac{\partial c_0}{\partial x} \left[\int_1^{+\infty} \left[\tilde{c}(x + \tilde{x}) + \tilde{c}(x - \tilde{x}) \right] I_1 \, \mathrm{d}\tilde{x} + \int_{-1}^{1} \tilde{c}(x + \tilde{x}) I_2 \, \mathrm{d}\tilde{x} \right],
\end{aligned}
\tag{4.3}
$$

where

$$
\begin{aligned}
I_1(\tilde{x}; k) &= \int_{-\infty}^{+\infty} \frac{\tilde{y}^2 - \tilde{x}^2}{(\tilde{x}^2 + \tilde{y}^2)^2} \cos(k\tilde{y}) \, \mathrm{d}\tilde{y} = -k \exp(-k\tilde{x}), \\
I_2(\tilde{x}; k) &= 2 \int_{-\infty}^{-\sqrt{1-\tilde{x}^2}} \frac{\tilde{y}^2 - \tilde{x}^2}{(\tilde{x}^2 + \tilde{y}^2)^2} \cos(k\tilde{y}) \, \mathrm{d}\tilde{y}.
\end{aligned}
\tag{4.4}
$$

Here, I_1 and I_2 constitute u_d in the Fourier space, while v_d=0 owing to the symmetry of the disturbance flow (i.e. $\boldsymbol{v}^{dip}$) and the uniformity of c_0 in the y-direction. The detailed derivation of (4.3) and (4.4) has been included in Appendix E.

Using the upwind numerical scheme, we compute $\tilde{c}(x, t)$ from (4.3), by assuming a Gaussian function with a particle-scale width as the initial condition. Once $\tilde{c}(x, t)$ is known, we define the growth rate σ based on the changes in the root mean square of $\tilde{c}(x, t)$ over the whole domain (Tan & Homsy 1986), or $\sigma \equiv \ln[M(t + \delta t) - M(t)]/\delta t$, where $M(t) \equiv \left[\int_{-L}^{L} [\tilde{c}(x, t)]^2 \, \mathrm{d}x/(2L) \right]^{1/2}$, with the time step δt and the domain size L. As shown in figure 3(*a*), σ varies non-monotonically with k and is positive for the intermediate values of k, while its overall magnitude decreases with time. In addition,

the critical wavenumber k_c at which $\partial\sigma/\partial k = 0$ gradually decreases over time, which corresponds to an increase in the critical wavelength λ_c with time. Hence our minimal model with inter-particle dipolar interactions correctly predicts widening of the emergent fingers with time at all particle concentrations. Note that our choice of initial data guarantees that a sufficiently wide range of Fourier modes is covered, and our specific definition of σ does not influence the wavenumber selection, which has been confirmed through numerical tests.

Furthermore, the behaviours of $\sigma(k;\, t)$ and k_c mirror those found in viscous fingering between two miscible fluids for low Pe. Tan & Homsy (1986) performed the stability analysis of the displacement of pure miscible liquids, and showed that thermal diffusion gradually increases the mixing region between the two fluids, which causes the finger width to widen over time. This striking similarity between our simulation results and the analysis by Tan & Homsy (1986) suggests that dipolar interactions between highly confined particles display the stabilising effects that are comparable to thermal diffusion even at $Pe \to \infty$.

However, distinct from Tan & Homsy (1986), our current model is not explicitly governed by the external parameters (e.g. Pe, viscosity ratios) that control the relative strength of stabilising and destabilising effects. Because the inter-particle dipolar interactions alone control the instability, the initial particle concentration drops out of the dimensionless equation, except to set the timescale of fingering. As the dimensionless time t has been normalised by ρ_i, our results indicate that the dimensional time $\hat{t} = td/(\kappa\pi S\rho_i)$ that it takes for the finger width to reach the comparable size must decrease with increasing ρ_i. Equivalently, at given dimensional time $\hat{t}$ that corresponds to longer t for larger ρ_i, the emergent fingers are predicted to be wider as ρ_i is increased, which is consistent with our experimental observations in figure 1(*c*).

For more quantitative comparison, we obtain the critical wavelengths λ_c from the experiments via image processing, which we describe in detail in Appendix B. We plot λ_c from the experiments as a function of t together with the numerical simulations in figure 3(*b*). Despite the scatter caused by the broad distribution of finger widths inside the rarefaction region, experimental λ_c increases with t and shows a reasonable collapse across all particle concentrations. Furthermore, the images in figure 3(*c*) from three separate experiments (i.e. $\phi_i = 5\,\%$, $15\,\%$, $25\,\%$) exhibit similar fingering patterns at given dimensionless time $t = 12$, which again qualitatively matches our model predictions.

4.3. *Mechanism of wavelength selection*

In our system, both experimental observations and linear stability analysis demonstrate the simultaneous development of rarefaction and fingering regions. To further elucidate the mechanism of wavelength selection via dipolar interactions, we focus on the $\partial c_0/\partial x$ term in (4.3), which directly addresses the viscosity contrast between the invading (clear oil) and defending (2-D suspension) phases. This term separates the current model from the work of Desreumaux *et al.* (2013), who performed a stability analysis on the 2-D uniform suspension flow. Their analysis yielded hydrodynamic fluctuations but no growing instabilities, which confirms that the $\partial c_0/\partial x$ term is indeed the key to viscous fingering. This choice is also confirmed by the ablation test included in Appendix F.

By systematically analysing the effects of the $\partial c_0/\partial x$ term on critical wavelength selection in (4.3), we reduce the governing equation for $\tilde{c}$ to

$$\frac{\partial \tilde{c}}{\partial t} + \frac{1}{\pi}\frac{\partial c_0}{\partial x}\int_1^{+\infty} \left[\tilde{c}(x+\tilde{x}) + \tilde{c}(x-\tilde{x})\right] I_1 \,\mathrm{d}\tilde{x} = 0. \tag{4.5}$$

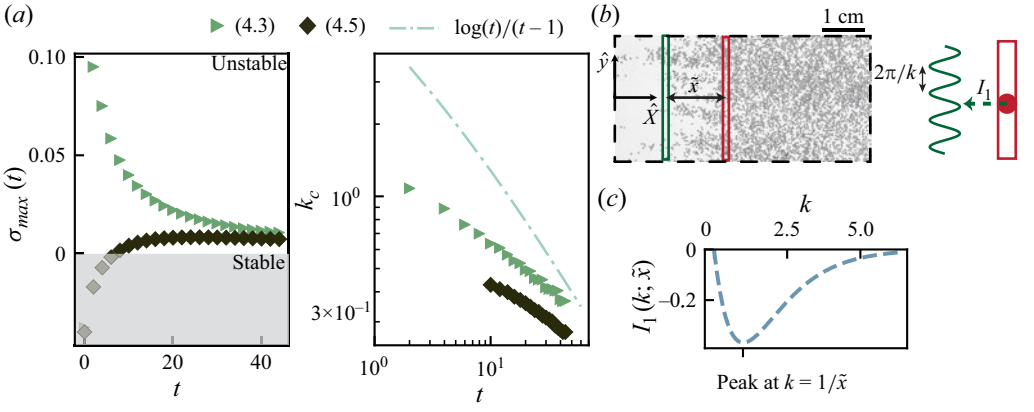

Figure 4. (*a*) Comparative simulation results between the comprehensive model (4.3) and the simplified physical model (4.5). The simplified model initially fails to capture the system's instability but converges to a similar constant maximum growth rate over long times. It also accurately predicts the broadening of the wavelength, or equivalently the decrease in k_c, as observed in the full model. (*b*) To represent the physical meaning of I_1, we include the schematic of the perturbed line of particles (green curve) affecting a test particle (red circle) placed at a distance $\tilde{x}$ away from it. (*c*) For given $\tilde{x}$, I_1 is negative for all k, and its magnitude reaches a maximum at $k = 1/\tilde{x}$. The wavenumber selection is influenced by the cumulative impact of all perturbed lines within the expanding rarefaction region.

We plot the maximum σ (i.e. σ_{max}) and k_c from (4.5), and compare them to the results of the full governing equation in figure 4(*a*), which shows a qualitative match with the full solutions as $t \to \infty$.

As illustrated in figure 4(*b*), $I_1(\tilde{x}; k)$ captures the effects of a column of perturbed particles (green line) on a 'test' particle (red circle) separated by a distance $\tilde{x}$. As shown in figure 4(*c*), for given $\tilde{x}$, I_1 is negative across all k, indicating that perturbing the green line will destabilise the test particle across all wavenumbers as long as $\partial c_0/\partial x > 0$. Additionally, for given $\tilde{x}$, the magnitude of I_1 peaks at $k = 1/\tilde{x}$, which implies that the perturbed green line selectively fosters the fastest-growing mode based on the separation distance.

As the product of I_1 and $\tilde{c}$ is integrated over $\tilde{x}$ in (4.5), the largest growing mode must be influenced by the size of the integration domain. The integration domain can be approximated as the rarefaction region, as our numerical solutions reveal that $\tilde{c}$ is mostly zero outside it. Finally, by assuming constant $\tilde{c}$ for simplicity, we integrate I_1 over the rarefaction region to obtain $k_c \propto \log(t)/(t-1)$. As shown in figure 4(*a*), this scaling decays more steeply with time compared to the full simulation results, which underscores the significance of accounting for the non-uniformity of $\tilde{c}$ within the rarefaction region. Despite the deviation between the scaling and the numerical results, our simple analysis illustrates that the expanding rarefaction region is the key to qualitatively capturing the decay of k_c, or the widening fingers, over time. The expanding rarefaction region parallels the growing mixing region between two miscible fluids, which explains the similarity between the x-component of the dipolar interactions and thermal diffusion that is responsible for generating the mixing region.

5. Conclusion

In this study, we experimentally demonstrate viscous fingering when pure oil displaces the mixture of the same oil and highly confined non-colloidal particles in the limit of zero

interfacial tension and diffusion. In contrast to other studies of miscible displacements at $Pe \to \infty$ (Videbæk & Nagel 2019; Luo *et al.* 2020; Videbæk 2020), our experiments show that fingers form at all particle concentrations, as the channel confinement eliminates the 3-D structure inside the channel gap that suppresses viscous fingering of all wavelengths. Furthermore, despite having no thermal diffusion, we find that fingering behaviours in 2-D suspensions are strongly reminiscent of classic 2-D viscous fingering between two miscible fluids at low Pe.

To rationalise this fingering regime, we develop a minimal mathematical model that captures the hydrodynamic interactions between the highly confined particles. Overall, our model successfully demonstrates that the dominant source of instability lies in the x-component of the dipolar interactions, initiating both the rarefaction wave and the subsequent instability along the y-direction. In addition, the expanding rarefaction region qualitatively takes on the role of 'diffusion', as it causes the critical finger width to widen over time. Because we do not have separate sources for fingering and stabilisation, our model is described by a universal equation that is independent of the particle concentration.

Our work combines viscous fingering with particle ensembles, which offers a new insight into harnessing instabilities to control the particle motion. For instance, strategically injecting the 2-D suspension to generate gradients in the particle concentration can lead to the shock or rarefaction waves and instabilities (Beatus, Tlusty & Bar-Ziv 2009), which will alter the emergent behaviours of particles. In addition to the control of particles, we will extend our current analysis by including more relevant physics into the model, such as the effects of the side walls, and investigating the coupling between fingering patterns and hydrodynamic fluctuations, as observed by Desreumaux *et al.* (2013). Finally, another future direction of research includes investigating the effects of channel confinement on the miscible displacement of a suspension with pure oil. The previous experiments by Luo *et al.* (2020) demonstrated that the miscible displacement of a suspension in the continuum limit completely deviates from the present monolayer limit. Hence it would be of great interest to characterise the onset of viscous fingering as the channel confinement is systematically varied from continuum to the monolayer limit.

Supplementary movie. Supplementary movie is available at https://doi.org/10.1017/jfm.2025.402.

Acknowledgements. The authors would like to acknowledge Z. Wang for helpful discussions, and R. Bansal for his help with the experiments.

Funding. R.L., M.M., Z.H. and S.L. are partly funded by the National Science Foundation (DMR-2003706, EAR-2100493). L.W. is partly supported by NSF DMS-1846854.

Declaration of interests. The authors report no conflict of interest.

Appendix A. Experimental procedure

To study the interfacial instability between the suspension and the clear oil, it is essential to establish an undisturbed, flat interface prior to the invasion of the clear oil into the suspension. This is achieved through the use of two 3-D-printed flow-guiding structures attached to either end of the Hele-Shaw cell. A suspension is prepared and injected through the structure designated as the suspension inlet into the Hele-Shaw cell. The injection continues until the suspension reaches the periphery of the cell, adjacent to the second structure. Once the suspension has filled the cell to the desired location, the suspension inlet is sealed to prevent any further inflow of suspension.

Clear oil is then injected into the reservoir of the second structure, ensuring that it makes contact with the suspension without causing any disturbances to the established interface.

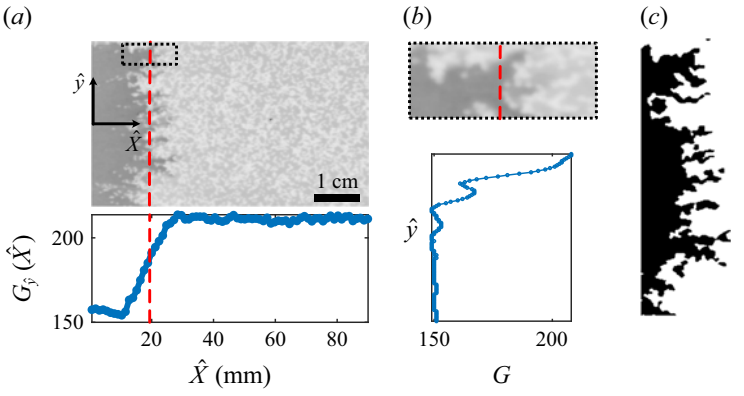

Figure 5. (*a*) The plot of the width-averaged intensity $G_y(\hat{X})$ as a function of $\hat{X}$ highlights the rarefaction region inside the cell. (*b*) We focus on the small region around the rarefaction region to highlight the variations of G in $\hat{y}$, corresponding to the emergent fingers. (*c*) We turn the original image into a binary image via thresholding (dyed oil in black), from which we extract λ_c.

The second structure comes with a circular opening on top, which allows air to vent out during initial oil injection. After the clear oil has been introduced, the circular opening (for releasing air) is sealed to maintain the integrity of the interface. With the circular opening sealed, the suspension inlet is reopened. Clear oil is injected again, this time invading the suspension and generating fingers. The displaced suspension is expelled through the suspension inlet, allowing for the observation of the interfacial instability as the clear oil advances.

Appendix B. Finger width measurements

We employ a fluorescent dye to visualise the flow patterns as silicone oil is injected into the mixture of the same oil and polystyrene particles. The captured images are processed using the red channel filter, denoted as $G(\hat{X}, \hat{y})$, to analyse the finger patterns (see figure 5*a*). The analysis proceeds as follows.

The rarefaction region is identified by calculating the $\hat{y}$-averaged intensity (grey scale) of the red channel, $G_y(\hat{X})$. The image is then cropped to focus on this region. As illustrated in figure 5(*b*), the intensity profile $G(\hat{y})$ along the centreline of the rarefaction region (red dashed line) reveals a distinct intensity variation, clearly demarcating the finger region. A fixed threshold is applied to the cropped image to extract the dyed oil region, resulting in a binary representation of the finger pattern (figure 5*c*). This binary image highlights the spatial distribution of the dyed oil within the rarefaction region. The finger pattern exhibits non-uniformity in both the $\hat{X}$- and $\hat{y}$-directions. In the $\hat{X}$-direction, the fingers are thinner near the front of the rarefaction region, and gradually widen towards the end. In the $\hat{y}$-direction, the width of the fingers varies due to the dynamic behaviour of the particles during injection. This non-uniformity is quantified by calculating the standard deviation of the finger width in the $\hat{y}$-direction, providing a measure of the spatial variability in the pattern.

Appendix C. Derivation of (3.3) and (3.4)

The key to deriving (3.3) from (3.2) is the simplification $\nabla \cdot \boldsymbol{j}$, where $\boldsymbol{j}$ is the dimensionless particle flux. Let us first introduce the relative position vector $\tilde{\boldsymbol{r}} = \boldsymbol{r}' - \boldsymbol{r}$,

where $\tilde{\boldsymbol{r}}$ denotes the displacement vector along the direction of the normal vector $\boldsymbol{n}$, such that $\tilde{\boldsymbol{r}} = (\tilde{x}, \tilde{y}) \cdot \boldsymbol{n}$. This definition is instrumental in simplifying the convection term and facilitating the physical interpretation of each term, as shown below:

$$\begin{aligned}
\nabla \cdot \boldsymbol{j}(\boldsymbol{r}, t) &= \nabla \cdot \left[\iint_{|\boldsymbol{r}-\boldsymbol{r}'|\geq 1} c(\boldsymbol{r}, t)\, \boldsymbol{v}^{dip}(\boldsymbol{r}, \boldsymbol{r}')\, c(\boldsymbol{r}', t)\, \mathrm{d}\boldsymbol{r}' \right] \\
&= \nabla c(\boldsymbol{r}, t) \cdot \iint_{|\boldsymbol{r}-\boldsymbol{r}'|\geq 1} \boldsymbol{v}^{dip}(\boldsymbol{r}, \boldsymbol{r}')\, c(\boldsymbol{r}', t)\, \mathrm{d}\boldsymbol{r}' + c(\boldsymbol{r}, t)\, \nabla \cdot \\
&\quad \left[\iint_{|\boldsymbol{r}-\boldsymbol{r}'|\geq 1} \boldsymbol{v}^{dip}(\boldsymbol{r}, \boldsymbol{r}')\, c(\boldsymbol{r}', t)\, \mathrm{d}\boldsymbol{r}' \right] \\
&= \frac{\partial c(\boldsymbol{r}, t)}{\partial x} \iint_{\tilde{x}^2+\tilde{y}^2\geq 1} \frac{\tilde{y}^2 - \tilde{x}^2}{(\tilde{x}^2+\tilde{y}^2)^2} c(x+\tilde{x}, y+\tilde{y}, t)\, \mathrm{d}\tilde{x}\mathrm{d}\tilde{y} \\
&\quad + \frac{\partial c(\boldsymbol{r}, t)}{\partial y} \iint_{\tilde{x}^2+\tilde{y}^2\geq 1} \frac{2\tilde{x}\tilde{y}}{(\tilde{x}^2+\tilde{y}^2)^2} c(x+\tilde{x}, y+\tilde{y}, t)\, \mathrm{d}\tilde{x}\mathrm{d}\tilde{y} - c(\boldsymbol{r}, t) \\
&\quad \times \int_0^{2\pi} c(\boldsymbol{r}-\boldsymbol{n}, t) \cos\theta\, \mathrm{d}\theta.
\end{aligned} \tag{C1}$$

Note that we have used the divergence theorem to simplify the following:

$$\begin{aligned}
\nabla \cdot \left[\iint_{|\boldsymbol{r}-\boldsymbol{r}'|\geq 1} \boldsymbol{v}^{dip}(\boldsymbol{r}, \boldsymbol{r}')\, c(\boldsymbol{r}', t)\, \mathrm{d}\boldsymbol{r}' \right] &= \iint_{|\tilde{\boldsymbol{r}}|\geq 1} \nabla_{\tilde{\boldsymbol{r}}} \cdot [\boldsymbol{v}^{dip}(\boldsymbol{r}, \boldsymbol{r}+\tilde{\boldsymbol{r}})\, c(\boldsymbol{r}+\tilde{\boldsymbol{r}}, t)]\, \mathrm{d}\tilde{\boldsymbol{r}} \\
&= -\int_{|\tilde{\boldsymbol{r}}|=1} \boldsymbol{v}^{dip}(\boldsymbol{r}, \boldsymbol{r}+\tilde{\boldsymbol{r}})\, c(\boldsymbol{r}+\tilde{\boldsymbol{r}}, t) \cdot \boldsymbol{n}\, \mathrm{d}\tilde{\boldsymbol{r}} \\
&= -\int_0^{2\pi} \boldsymbol{v}^{dip}(\boldsymbol{r}, \boldsymbol{r}+\boldsymbol{n}) \cdot \hat{n}\, c(\boldsymbol{r}+\boldsymbol{n}, t)\, \mathrm{d}\theta \\
&= -\int_0^{2\pi} c(\boldsymbol{r}-\boldsymbol{n}, t) \cos\theta\, \mathrm{d}\theta\,.
\end{aligned} \tag{C2}$$

Inserting (C1) into the original conservation law leads to (3.3)–(3.4), which govern the evolution of particle concentration.

Another major step in deriving (3.3) is the coordinate transformation based on $\hat{x} = \hat{X} - \kappa(\hat{v}^{\infty} + \pi S\rho_i)\hat{t}$ and non-dimensionalisation via $\hat{x} = xd$, $\hat{t} = t(d/\kappa\pi S\rho_i)$:

$$\begin{aligned}
\frac{\partial \rho(\hat{X}, \hat{y}, \hat{t})}{\partial \hat{t}} &= \rho_i \frac{\partial c(\hat{X}, \hat{y}, \hat{t})}{\partial \hat{t}} \\
&= \rho_i \frac{\partial c(\hat{x}, \hat{y}, \hat{t})}{\partial \hat{x}} \frac{\partial \hat{x}}{\partial \hat{t}} + \rho_i \frac{\partial c(\hat{x}, \hat{y}, \hat{t})}{\partial \hat{t}} \\
&= \rho_i \frac{\partial c(\hat{x}, \hat{y}, \hat{t})}{\partial \hat{t}} - \kappa\pi S\rho_i^2 \frac{\partial c(\hat{x}, \hat{y}, \hat{t})}{\partial \hat{x}} - \kappa \hat{v}^{\infty} \frac{\partial c(\hat{x}, \hat{y}, \hat{t})}{\partial \hat{x}} \\
&= \frac{\kappa\pi S\rho_i^2}{d} \frac{\partial c(x, y, t)}{\partial t} - \frac{\kappa\pi S\rho_i^2}{d} \frac{\partial c(x, y, t)}{\partial x} - \kappa \hat{v}^{\infty} \frac{\partial c(x, y, t)}{\partial x}.
\end{aligned} \tag{C3}$$

Appendix D. Derivation of (4.1)

The leading order equation is obtained from (3.3) by introducing decomposition $c{=}c_0(x,t)+\delta\, c(x,\,y,\,t)$, where $|c_0|{\gg}|\delta c|$, and keeping the terms with c_0,

$$\frac{\partial c_0}{\partial t}+\left(\frac{1}{\pi}u_{\mathrm{d}}^0-1\right)\frac{\partial c_0}{\partial x}+\frac{1}{\pi}v_{\mathrm{d}}^0\cancelto{0}{\frac{\partial c_0}{\partial y}}-\frac{1}{\pi}c_0\int_0^{2\pi}c_0(x-\cos\theta,t)\cos\theta\,\mathrm{d}\theta=0, \tag{D1}$$

where

$$\begin{aligned}u_d^0(x)&=\iint_{\tilde{x}^2+\tilde{y}^2\geq 1}\frac{\tilde{y}^2-\tilde{x}^2}{(\tilde{x}^2+\tilde{y}^2)^2}c_0(x+\tilde{x},\,t)\,\mathrm{d}\tilde{x}\mathrm{d}\tilde{y},\\ v_d^0(x)&=\iint_{\tilde{x}^2+\tilde{y}^2\geq 1}\frac{2\tilde{x}\tilde{y}}{(\tilde{x}^2+\tilde{y}^2)^2}c_0(x+\tilde{x},\,t)\,\mathrm{d}\tilde{x}\mathrm{d}\tilde{y}.\end{aligned} \tag{D2}$$

Here, $u_d^0(x)$ is further divided into four regions to compute the integral:

$$\begin{aligned}u_{\mathrm{d}}^0(x)=&\int_{-\infty}^{-1}c_0(x+\tilde{x},t)\mathrm{d}\tilde{x}\cancelto{0}{\int_{-\infty}^{\infty}\frac{\tilde{y}^2-\tilde{x}^2}{(\tilde{x}^2+\tilde{y}^2)^2}\,\mathrm{d}\tilde{y}}+\int_1^{\infty}c_0(x+\tilde{x},t)\mathrm{d}\tilde{x}\cancelto{0}{\int_{-\infty}^{\infty}\frac{\tilde{y}^2-\tilde{x}^2}{(\tilde{x}^2+\tilde{y}^2)^2}\,\mathrm{d}\tilde{y}}\\ &+\int_{-1}^{1}c_0(x+\tilde{x},t)\int_{-\infty}^{-1}\frac{\tilde{y}^2-\tilde{x}^2}{(\tilde{x}^2+\tilde{y}^2)^2}\,\mathrm{d}\tilde{y}\mathrm{d}\tilde{x}+\int_{-1}^{1}c_0(x+\tilde{x},t)\int_1^{\infty}\frac{\tilde{y}^2-\tilde{x}^2}{(\tilde{x}^2+\tilde{y}^2)^2}\,\mathrm{d}\tilde{y}\mathrm{d}\tilde{x}\\ =&\,2\int_{-1}^{1}c_0(x+\tilde{x},t)\sqrt{1-\tilde{x}^2}\,\mathrm{d}\tilde{x}.\end{aligned} \tag{D3}$$

Now we apply the Taylor expansion of $c_0(x+\tilde{x},\,t)\approx c_0(x,\,t)+\partial_x c_0(x,\,t)\tilde{x}$ to obtain

$$u_{\mathrm{d}}^0(x)\approx 2c_0(x,t)\int_{-1}^{1}\sqrt{1-\tilde{x}^2}\,\mathrm{d}\tilde{x}+2\frac{\partial c_0(x,t)}{\partial x}\cancelto{0}{\int_{-1}^{1}\tilde{x}\sqrt{1-\tilde{x}^2}\,\mathrm{d}\tilde{x}}=\pi c_0, \tag{D4}$$

and

$$\int_0^{2\pi}c_0(x-\cos\theta,t)\cos\theta\,\mathrm{d}\theta\approx c_0(x,t)\cancelto{0}{\int_0^{2\pi}\cos\theta\,\mathrm{d}\theta}-\frac{\partial c_0(x,t)}{\partial x}\int_0^{2\pi}\cos^2\theta\,\mathrm{d}\theta=-\pi\frac{\partial c_0}{\partial x}. \tag{D5}$$

Appendix E. Derivation of (4.3) and (4.4)

The perturbation equation for $\delta\, c(x,\,y,\,t)$ is

$$\begin{aligned}0=&\frac{\partial\delta c(x,y,t)}{\partial t}+\frac{1}{\pi}u^{(1)}\frac{\partial c_0(x,t)}{\partial x}+\frac{1}{\pi}u^{(0)}\frac{\partial\delta c(x,y,t)}{\partial x}+\frac{1}{\pi}v^{(1)}\cancelto{0}{\frac{\partial c_0(x,t)}{\partial y}}\\ &+\frac{1}{\pi}\frac{\partial\delta c(x,y,t)}{\partial y}\cancelto{0}{v^{(0)}}-\frac{1}{\pi}c_0g(\delta c)-\frac{1}{\pi}\delta c(x,y,t)g(c_0),\end{aligned} \tag{E1}$$

where $v^{(0)}=\iint_{\tilde{x}^2+\tilde{y}^2\geq 1}(2\tilde{x}\tilde{y}/(\tilde{x}^2+\tilde{y}^2)^2)\,c_0(x+\tilde{x},\,t)\,\mathrm{d}\tilde{x}\mathrm{d}\tilde{y}=0$, $g(c_0)=\int_0^{2\pi}c_0(x-\cos\theta,\,t)\cos\theta\,\mathrm{d}\theta$, $g(\delta c)=\int_0^{2\pi}\delta\, c(\boldsymbol{r}-\boldsymbol{n},\,t)\cos\theta\,\mathrm{d}\theta$. Additionally,

$$u^{(1)}=\iint_{\tilde{x}^2+\tilde{y}^2\geq 1}\frac{\tilde{y}^2-\tilde{x}^2}{(\tilde{x}^2+\tilde{y}^2)^2}\delta\, c(x+\tilde{x},\,y+\tilde{y},\,t)\,\mathrm{d}\tilde{y}\mathrm{d}\tilde{x}. \tag{E2}$$

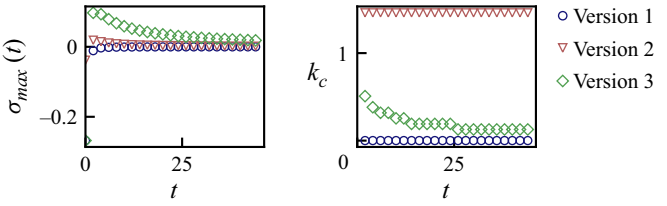

Figure 6. The maximum growth rate ($\sigma_{max}(t)$) and critical wavenumber (k_c) over time based on versions 1, 2, 3 of (4.3).

By setting $\delta c(x, y, t) \equiv 2\sum_k \tilde{c}(x, t)\cos(ky)$ with the wavenumber k and plugging it into (E1), we rewrite the double integral in (E2) as

$$\begin{aligned}
u^{(1)}/\cos(ky) &= \iint_{\tilde{x}^2+\tilde{y}^2\geq 1} \frac{\tilde{y}^2-\tilde{x}^2}{(\tilde{x}^2+\tilde{y}^2)^2}\tilde{c}(x+\tilde{x}, t)\cos(k\tilde{y})\,\mathrm{d}\tilde{x}\mathrm{d}\tilde{y} \\
&= \int_{-\infty}^{-1}\tilde{c}(x+\tilde{x}, t)\int_{-1}^{1}\frac{\tilde{y}^2-\tilde{x}^2}{(\tilde{x}^2+\tilde{y}^2)^2}\cos(k\tilde{y})\,\mathrm{d}\tilde{y}\mathrm{d}\tilde{x} \\
&\quad + \int_{1}^{+\infty}\tilde{c}(x+\tilde{x}, t)\int_{-1}^{1}\frac{\tilde{y}^2-\tilde{x}^2}{(\tilde{x}^2+\tilde{y}^2)^2}\cos(k\tilde{y})\,\mathrm{d}\tilde{y}\mathrm{d}\tilde{x} \\
&\quad + \int_{-1}^{+1}\tilde{c}(x+\tilde{x}, t)\int_{-\infty}^{-\sqrt{1-\tilde{x}^2}}\frac{\tilde{y}^2-\tilde{x}^2}{(\tilde{x}^2+\tilde{y}^2)^2}\cos(k\tilde{y})\,\mathrm{d}\tilde{y}\mathrm{d}\tilde{x} \\
&\quad + \int_{-1}^{+1}\tilde{c}(x+\tilde{x}, t)\int_{\sqrt{1-\tilde{x}^2}}^{+\infty}\frac{\tilde{y}^2-\tilde{x}^2}{(\tilde{x}^2+\tilde{y}^2)^2}\cos(k\tilde{y})\,\mathrm{d}\tilde{y}\mathrm{d}\tilde{x} \\
&= \int_{1}^{+\infty}\left[\tilde{c}(x+\tilde{x}, t)+\tilde{c}(x-\tilde{x}, t)\right]\int_{-\infty}^{\infty}\frac{\tilde{y}^2-\tilde{x}^2}{(\tilde{x}^2+\tilde{y}^2)^2}\cos(k\tilde{y})\,\mathrm{d}\tilde{y}\mathrm{d}\tilde{x} \\
&\quad + 2\int_{-1}^{+1}\tilde{c}(x+\tilde{x}, t)\int_{-\infty}^{-\sqrt{1-\tilde{x}^2}}\frac{\tilde{y}^2-\tilde{x}^2}{(\tilde{x}^2+\tilde{y}^2)^2}\cos(k\tilde{y})\,\mathrm{d}\tilde{y}\mathrm{d}\tilde{x}.
\end{aligned} \tag{E3}$$

This expression reveals the cumulative impact of particles within the rarefaction zone (i.e. $\partial c_0/\partial x \neq 0$) and sets our current model apart from the one for the uniform suspension described by Desreumaux *et al.* (2013).

Appendix F. Ablation test

We conduct an ablation test by systematically deleting selected terms from (4.3), and numerically determining the maximum growth rate (σ_{max}) and critical wavenumber (k_c). We consider the following three versions of (4.3). Version 1 consists of all the terms of (4.3), except for the last two integral terms, which contain $(1/\pi)\,\partial c_0/\partial x$. This version of (4.3) is consistent with the model by Desreumaux *et al.* (2013) when c_0 is constant. Version 2 is only missing $(1/\pi)(\partial c_0/\partial x)\left[\int_1^{+\infty}[\tilde{c}(x+\tilde{x})+\tilde{c}(x-\tilde{x})]I_1\,\mathrm{d}\tilde{x}\right]$ from (4.3), while version 3 does not contain $(1/\pi)(\partial c_0/\partial x)[\int_{-1}^{1}\tilde{c}(x+\tilde{x})I_2\,\mathrm{d}\tilde{x}]$ only. The plots in figure 6 demonstrate the importance of the term $(1/\pi)(\partial c_0/\partial x)\left[\int_1^{+\infty}[\tilde{c}(x+\tilde{x})+\tilde{c}(x-\tilde{x})\right]I_1\,\mathrm{d}\tilde{x}]$. Namely, only version 3 of the governing equation that retains this term shows the decay of k_c over time, which qualitatively matches the full numerical results from solving (4.3).

References

Beatus, T., Bar-Ziv, R.H. & Tlusty, T. 2012 The physics of 2D microfluidic droplet ensembles. *Phys. Rep.* **516** (3), 103–145.

Beatus, T., Tlusty, T. & Bar-Ziv, R. 2006 Phonons in a one-dimensional microfluidic crystal. *Nat. Phys.* **2** (11), 743–748.

Beatus, T., Tlusty, T. & Bar-Ziv, R. 2009 Burgers shock waves and sound in a 2D microfluidic droplets ensemble. *Phys. Rev. Lett.* **103** (11), 114502.

Bischofberger, I., Ramachandran, R. & Nagel, S.R. 2014 Fingering versus stability in the limit of zero interfacial tension. *Nat. Commun.* **5** (1), 5265.

Booth, R.J.S. 2010 On the growth of the mixing zone in miscible viscous fingering. *J. Fluid Mech.* **655**, 527–539.

Brady, J.F. 1983 The Einstein viscosity correction in *n* dimensions. *Intl J. Multiphase Flow* **10** (1), 113–114.

Chuoke, R.L., van Meurs, P. & van der Poel, C. 1959 The instability of slow, immiscible, viscous liquid–liquid displacements in permeable media. *Trans. AIME* **216** (1), 188–194.

Couder, Y. 2000 Viscous fingering as an archetype for growth patterns. In *Perspectives in Fluid Dynamics* (ed. G.K. Batchelor, H.K. Moffatt & M.G. Worster), pp. 53–104. Cambridge University Press.

Delmotte, B., Driscoll, M., Chaikin, P. & Donev, A. 2017 Hydrodynamic shocks in microroller suspensions. *Phys. Rev. Fluids* **2** (9), 092301.

Desreumaux, N., Caussin, J.-B., Jeanneret, R., Lauga, E. & Bartolo, D. 2013 Hydrodynamic fluctuations in confined particle-laden fluids. *Phys. Rev. Lett.* **111** (11), 118301.

Driscoll, M., Delmotte, B., Youssef, M., Sacanna, S., Donev, A. & Chaikin, P. 2017 Unstable fronts and motile structures formed by microrollers. *Nat. Phys.* **13** (4), 375–379.

Einstein, A. 1906 Eine neue Bestimmung der Moleküldimensionen. *Ann. Phys.* **324** (2), 289–306.

Goyal, N. & Meiburg, E. 2006 Miscible displacements in Hele-Shaw cells: two-dimensional base states and their linear stability. *J. Fluid Mech.* **558**, 329.

Hickernell, F.J. & Yortsos, Y.C. 1986 Linear stability of miscible displacement processes in porous media in the absence of dispersion. *Stud. Appl. Maths* **74** (2), 93–115.

Homsy, G.M. 1987 Viscous fingering in porous media. *Annu. Rev. Fluid Mech.* **19** (1), 271–311.

Luo, R., Chen, Y. & Lee, S. 2020 Particle-induced miscible fingering: continuum limit. *Phys. Rev. Fluids* **5** (9), 094301.

Menzel, A.M. 2012 Collective motion of binary self-propelled particle mixtures. *Phys. Rev. E* **85** (2), 021912.

Nijjer, J.S., Hewitt, D.R. & Neufeld, J.A. 2018 The dynamics of miscible viscous fingering from onset to shutdown. *J. Fluid Mech.* **837**, 520–545.

Park, C.-W., Gorell, S. & Homsy, G.M. 1984 Two-phase displacement in Hele-Shaw cells: experiments on viscously driven instabilities. *J. Fluid Mech.* **141**, 275–287.

Park, C.-W. & Homsy, G.M. 1984 Two-phase displacement in Hele-Shaw cells: theory. *J. Fluid Mech.* **139**, 291–308.

Saffman, P.G. & Taylor, G. 1958 The penetration of a fluid into a porous medium or Hele-Shaw cell containing a more viscous liquid. *Proc. R. Soc. Lond. A: Math. Phys. Sci.* **1242**, 312–329.

Sprinkle, B., Wilken, S., Karapetyan, S., Tanaka, M., Chen, Z., Cruise, J.R., Delmotte, B., Driscoll, M.M., Chaikin, P. & Donev, A. 2021 Sedimentation of a colloidal monolayer down an inclined plane. *Phys. Rev. Fluids* **6** (3), 034202.

Tan, C.T. & Homsy, G.M. 1986 Stability of miscible displacements in porous media: rectilinear flow. *Phys. Fluids* **29** (11), 3549–3556.

Videbæk, T.E. 2020 Delayed onset and the transition to late time growth in viscous fingering. *Phys. Rev. Fluids* **5** (12), 123901.

Videbæk, T.E. & Nagel, S.R. 2019 Diffusion-driven transition between two regimes of viscous fingering. *Phys. Rev. Fluids* **4** (3), 033902.

Wooding, R.A. 1962 The stability of an interface between miscible fluids in a porous medium. *Zeitschrift fur angewandte Mathematik und Physik* **13** (3), 255–266.

Yortsos, Y.C. & Salin, D. 2006 On the selection principle for viscous fingering in porous media. *J. Fluid Mech.* **557**, 225.